# Supporting Information

## Single-shot multiparametric MRI for separating $T_2$ effects from dynamic glucose-enhanced contrast

Junxian Jin[1], Haizhen Ding[2], Zhekai Chen[1], Yuan Huang[1], Hongmin Chen[2], Zhong Chen[1*], Lin Chen[1*]

1 Department of Electronic Science, Fujian Provincial Key Laboratory of Plasma and Magnetic Resonance, School of Electronic Science and Engineering, National Model Microelectronics College, Xiamen University, Xiamen, China

2 State Key Laboratory of Vaccines for Infectious Diseases, Xiang An Biomedicine Laboratory, National Innovation Platform for Industry-Education Integration in Vaccine Research, School of Public Health, Xiamen University, Xiamen, China

*Corresponding Author:

Lin Chen

Xiamen University, Xiamen, China

E-mail: chenlin21@xmu.edu.cn

Zhong Chen

Xiamen University, Xiamen, China

E-mail: chenz@xmu.edu.cn

**Supplementary Section 1. Data processing workflow**

The corresponding workflow for generating the $T_2$ and PD maps is illustrated in **Figure S1**. A one-dimensional Fourier transform was first applied along the readout dimension. Even and odd echo train datasets were then separated and individually processed using a super-resolution transformation to correct for blurring caused by parabolic phase profiles [1]. A self-referenced correction step was incorporated to mitigate gradient system imperfections and motion-related artifacts [2]. To ensure consistent image orientation, images from even echoes were flipped due to the opposite spatial rasterization directions along the SPEN dimension. Effective echo times ($TE_{eff}$) were calculated based on the spatial position along the SPEN axis. Finally, voxel-wise mono-exponential fitting was performed using Eq. 4 to derive quantitative $T_2$ and PD maps.

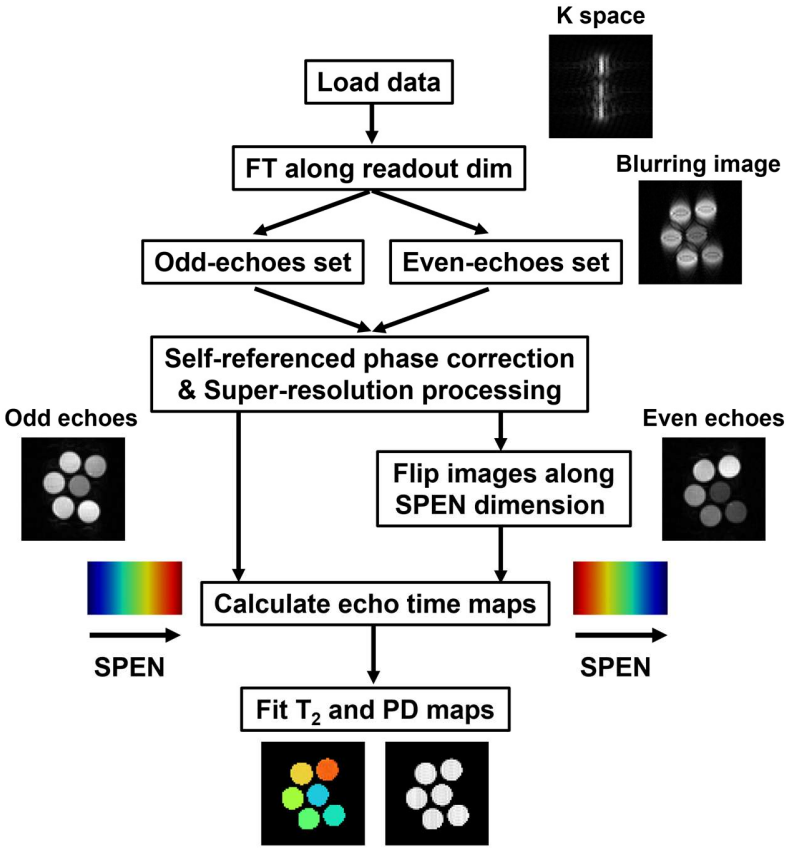


**Figure S1**. Data processing workflow for generating $T_2$ and PD maps from MP-CEST imaging.

A representative fitting result from one of the phantoms is shown in **Figure S2**. The fitted curve demonstrated satisfactory agreement with the acquired multi-echo data, yielding $T_2$ and normalized PD fitting errors within ±1.5 ms and 2%, respectively (**Figure S2A and Table S4**). Residual analysis further validated the reliability of the fitting, with deviations between the measured and fitted signal intensities remaining below 2.5% across all data points (**Figure S2B**).

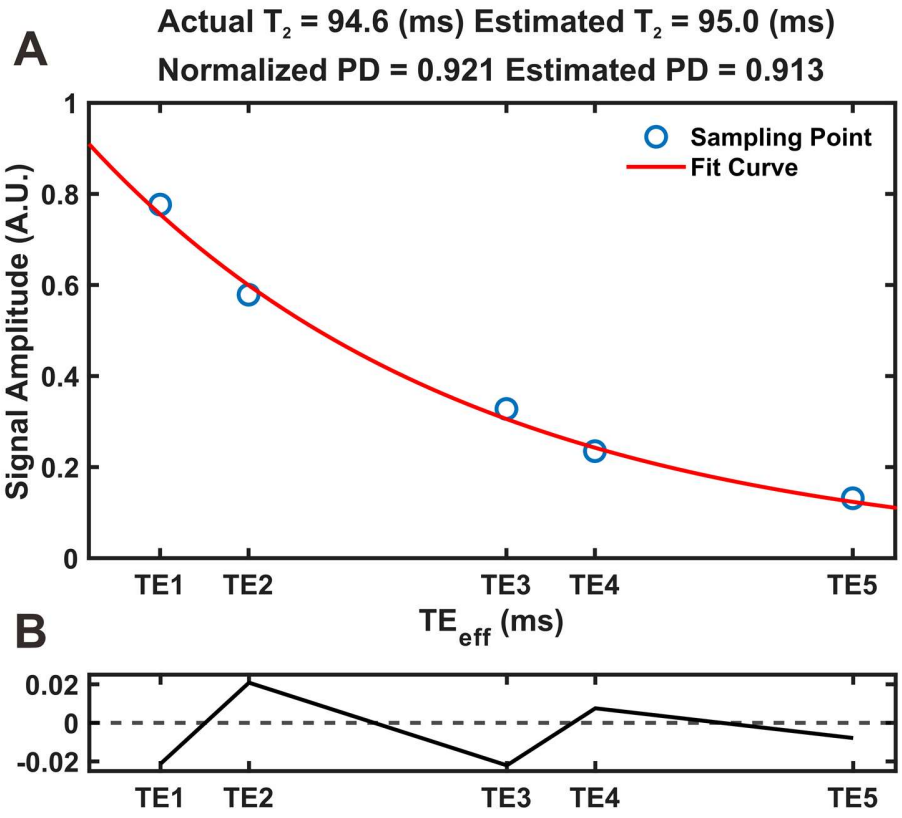


**Figure S2**. Representative results of $T_2$ and PD fitting and residual analysis. **(A)** Multi-echo signal intensities (dots) and the corresponding voxel-wise mono-exponential fitting curve (line) from one phantom voxel. **(B)** Residuals between the measured and fitted signals, demonstrating fitting accuracy within 2.5%.

**Supplementary Section 2. Validation of model robustness and generalizability**

Details regarding the calibration parameters a, b, c, and k are provided, including the fitting procedure and the assessment of parameter stability. In addition, we extended the validation of the proposed model by incorporating both numerical simulations and phantom experiments to evaluate its robustness and generalizability.

**Table S1**. Simulation parameter settings used to generate $T_2$ correction coefficients based on the Bloch–McConnell model.

| **Parameters for generating correction parameters** | | | |
|---|---|---|---|
| **Category / Condition** | **Phantom** | **Brain** | **Tumor** |
| $B_0$ | 7 T | 7 T | 7 T |
| Saturation power | 2 μT | 2 μT | 2 μT |
| Saturation length | 2 s | 2 s | 2 s |
| Z-spectral range | -5 ~ 5 ppm | -5 ~ 5 ppm | -5 ~ 5 ppm |
| Glucose pool | 1.2 ppm | 1.2 ppm | 1.2 ppm |
| Glucose exchange rate | 1600 Hz | 1600 Hz | 1600 Hz |
| Glucose concentration | 50 mM | 2 mM | 2 mM |
| $T_1$ | 2.5 s | 1.5 s | 1.67 s |
| $T_2$ | 25 ~ 500 ms | 25 ~ 70 ms | 25 ~ 100 ms |
| $f_{MTC}$ | —— | 5% | 2% |
| $T_{2,MTC}$ | —— | 0.0091 ms | 0.0091 ms |
| $k_{MTC}$ | —— | 40 Hz | 40 Hz |
| MTC offset | —— | 0 ppm | 0 ppm |
| MTC lineshape | —— | Super-Lorentzian | Super-Lorentzian |

To validate the relationship between $\Delta T_2$ and background-induced signal changes described in Eqs. 16 and 19, numerical simulations were performed using phantom-matched parameters

(summarized in **Table S1**), with a baseline $T_2$ of 50 ms and a glucose concentration of 50 mM. The resulting background-induced $\Delta S/S_0$ and $\Delta MTR_{asym}$ changes as functions of $\Delta T_2$ are shown in **Figure S3**. As illustrated, $\Delta S/S_0$ exhibits an approximately linear relationship with $\Delta T_2$, while $\Delta MTR_{asym}$ demonstrates a quadratic dependence.

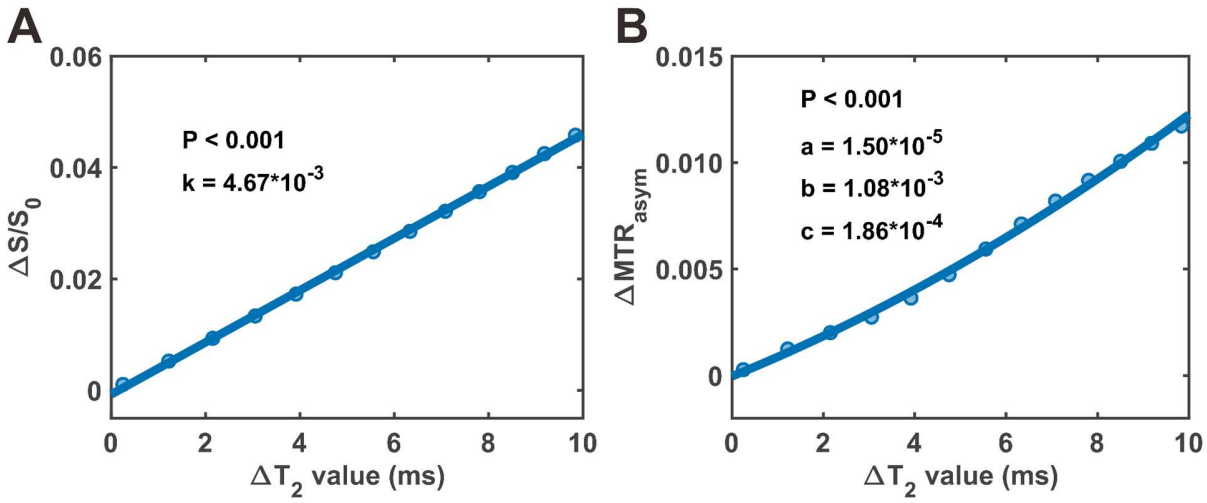


**Figure S3**. Background-induced signal changes in CEST quantification as a function of $\Delta T_2$. **(A)** $\Delta S/S_0$ as a function of $\Delta T_2$, along with the fitted calibration curve. **(B)** $\Delta MTR_{asym}$ as a function of $\Delta T_2$ variation, along with the fitted calibration curve.

## Effect of $\Delta T_2$ on background-induced signal changes across broader frequency offsets

**Figure S4** shows the dependence of background-induced $\Delta S/S_0$ and $\Delta MTR_{asym}$ on $\Delta T_2$ at a fixed glucose concentration across different frequency offsets. **Figure S4A–D** shows that $\Delta S/S_0$ exhibits an approximately linear relationship with $\Delta T_2$, while **Figure S4E–H** demonstrates a quadratic dependence of $\Delta MTR_{asym}$ on $\Delta T_2$. Notably, although the $\Delta MTR_{asym}$ signal decreases as the frequency offset moves farther from the glucose resonance at 1.2 ppm, it still reflects a second-order relationship due to the persistent influence of the scaled-down effect.

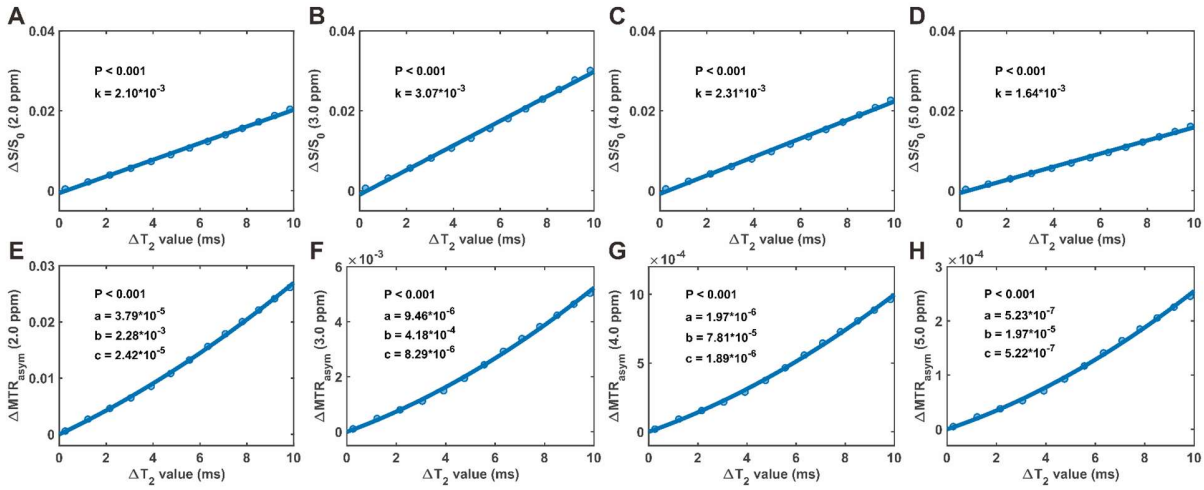


**Figure S4**. **(A-D)** $\Delta S/S_0$ as a function of $\Delta T_2$, along with the fitted calibration curve at 2 ppm, 3 ppm, 4 ppm, and 5 ppm, respectively. **(E-H)** $\Delta MTR_{asym}$ as a function of $\Delta T_2$ variation, along with the fitted calibration curve at 2 ppm, 3 ppm, 4 ppm, and 5 ppm.

To validate the reliability of the correction parameters, additional simulations were conducted to assess the robustness of the $T_2$ correction model against physiological variations in T1, MTC fraction, and glucose concentration, as shown in **Figure S5**. The simulated background-induced $\Delta S/S_0$ and $\Delta MTR_{asym}$ values exhibited excellent resistance to changes in these parameters. Specifically, when $T_1$ varied from 1200 ms to 1800 ms, $\Delta S/S_0$ showed a relative difference of 3.45% (from $0.030 \pm 0.0031$ to $0.028 \pm 0.0034$), and $\Delta MTR_{asym}$ varied by 3.51% (from $0.0055 \pm 0.00094$ to $0.0059 \pm 0.00079$). With an increase in MTC fraction from 1% to 3%, $\Delta S/S_0$ decreased by 8.77% (from $0.031 \pm 0.0046$ to $0.026 \pm 0.0035$), and $\Delta MTR_{asym}$ decreased by 13.33% (from $0.0068 \pm 0.00076$ to $0.0052 \pm 0.00056$). In comparison, varying the glucose concentration from 1 mM to 3 mM had a negligible impact on $\Delta S/S_0$ (both remained at 0.035), while $\Delta MTR_{asym}$ increased from $0.0011 \pm 0.00017$ to $0.0034 \pm 0.00062$. Although the relative percentage change is larger, the absolute magnitude of $\Delta MTR_{asym}$ remains small, and thus is unlikely to compromise the correction accuracy. These findings confirm the robustness and reliability of the proposed $T_2$ correction model across a physiologically relevant parameter space, underscoring its applicability in dynamic glucose-enhanced imaging.

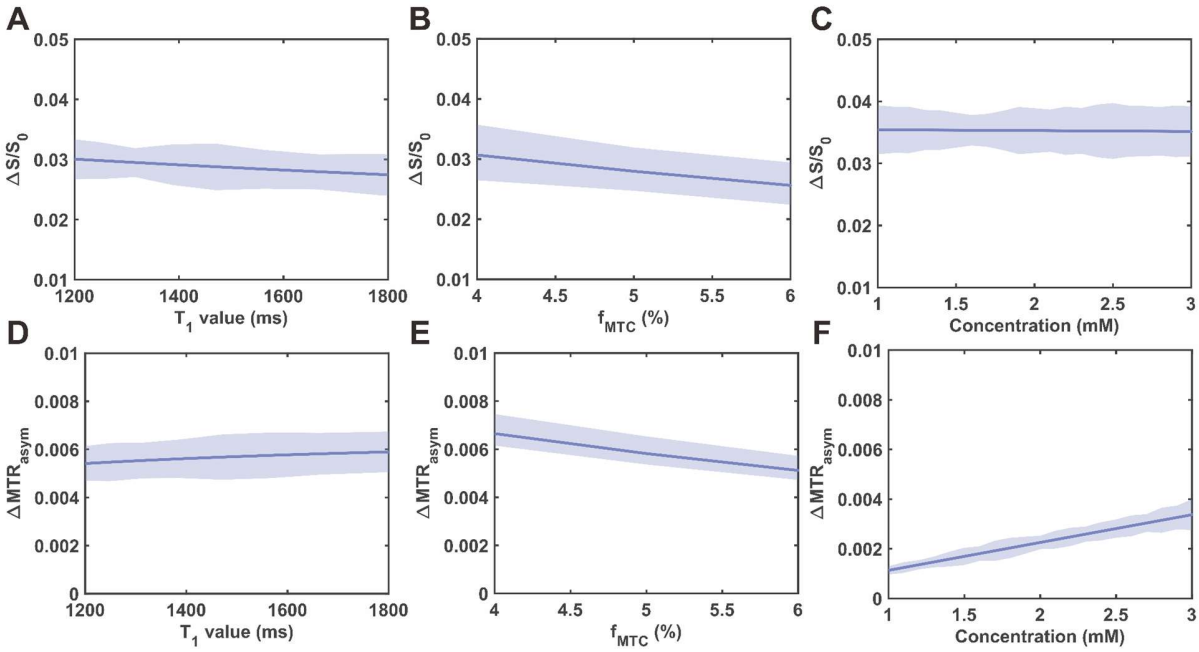


**Figure S5**. Simulation results showing that the $T_2$ correction model yields robust performance across a range of $T_1$ values, MTC fractions, and glucose concentrations. The exchange rate, baseline $T_2$, and $\Delta T_2$ were set to 1600 Hz, 50 ms, and 10 ms. The remaining simulation parameters are listed in **Table S1**. Background-induced **(A-C)** $\Delta S/S_0$ and **(D–F)** $\Delta MTR_{asym}$ as a function of varying (A, D) $T_1$ values (1200–1800 ms), (B, E) MTC pool fractions ($f_{MTC}$, 4%–6%), and (C, F) glucose concentrations (1–3 mM).

## *In vitro* validation of $T_2$ correction

Quantification maps at varying glucose concentrations acquired using MP-CEST are presented in **Figure S6C**. As glucose concentration increased, $S/S_0$ decreased near the 1.2 ppm offset, whereas $MTR_{asym}$ showed a corresponding increase (**Figure S6A-B**). Quantitative analysis revealed a linear inverse relationship between glucose concentration and $S/S_0$, while $MTR_{asym}$ exhibited a second-order dependence under physiological conditions (**Figure S6D and S6F**), consistent with simulation results. After $T_2$ correction, the linear correlation between glucose concentration and $S/S_0$ was attenuated **(Figure S6E)**, indicating effective suppression of $T_2$-dependent spillover effects. In contrast, $MTR_{asym}$ demonstrated a linear positive correlation with

glucose concentration post-correction (**Figure S6G**), further supporting the correction's ability to minimize $T_2$-related confounds. It is important to note that $T_2$ correction requires the definition of a baseline $T_2$ value, which, in the phantom experiments, was assumed to correspond to the phantom with the highest $T_2$ (i.e., the lowest glucose concentration).

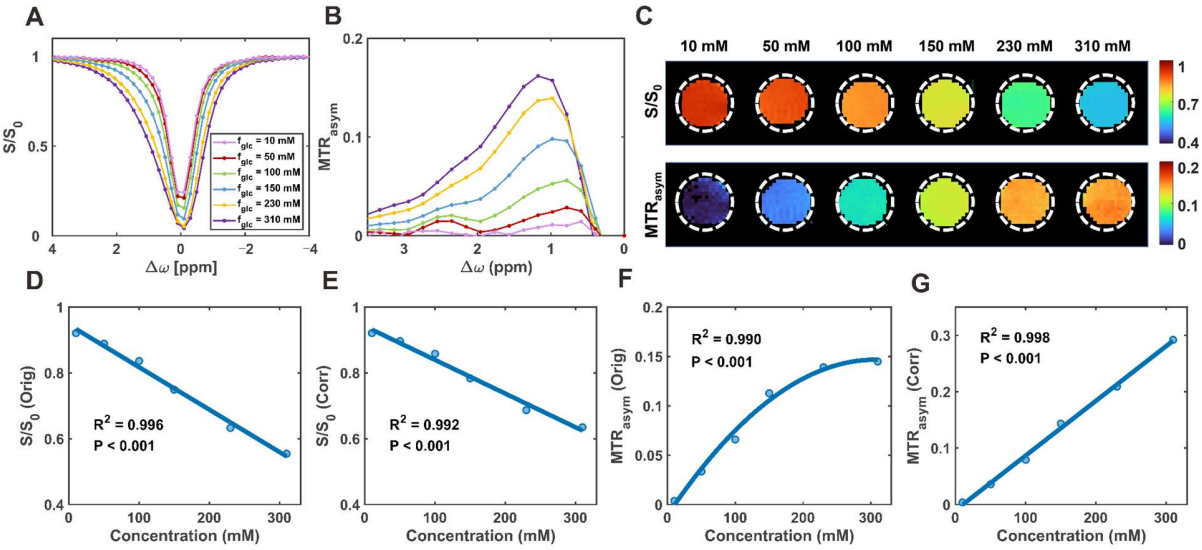


**Figure S6**. **(A)** Representative Z-spectra acquired from phantoms with different glucose concentrations. **(B)** Corresponding $MTR_{asym}$ curves calculated from the spectra in (A). **(C)** Quantitative maps generated from saturation-weighted PD images prior to $T_2$ correction. **(D)** Correlation between glucose concentration and normalized signal intensity $S/S_0$ before $T_2$ correction. **(E)** Correlation between glucose concentration and normalized signal intensity $S/S_0$ after $T_2$ correction. **(F)** Correlation between glucose concentration and $MTR_{asym}$ before $T_2$ correction. **(G)** Correlation between glucose concentration and $MTR_{asym}$ after $T_2$ correction.

**Supplementary Section 3. Numerical simulation details**

The synthetic Z-spectra were generated using Bloch–McConnell equations to simulate the CEST effect under varying $T_2$ and glucose concentration conditions. All simulations were performed using custom MATLAB scripts, assuming two-pool exchange between water and solute protons. The specific parameters used for the simulations are summarized in Supplementary **Table S2**.

**Table S2**. Parameter settings for simulating $T_2$ and glucose concentration effects using the Bloch–McConnell model.

| Parameters for generating Z-spectrum | |
|---|---|
| $B_0$ | 7 T |
| Saturation power | 2 μT |
| Saturation length | 2 s |
| $T_1$ | 2.5 s |
| Z-spectral range | -5 ~ 5 ppm |
| Glucose pool | 1.2 ppm |
| Glucose exchange rate | 1600 Hz |
| Glucose concentration | 0 ~ 500 mM |
| $R_2$ | 10 ~ 36.5 $s^{-1}$ |
| $r_{2ex,\ glc}$ | 0.053 $s^{-1}$ $mM^{-1}$ |

**Supplementary Section 4. Optimization of echo spacing and number of echoes**

In this study, a 5-echo train with an echo spacing of 25 ms was employed in the MP-CEST sequence. For the *in vivo* rat brain and tumor xenograft models, the typical $T_2$ values range from approximately 30 to 60 ms in healthy brain tissue and extend up to 100 ms in tumor regions. To ensure accurate $T_2$ quantification across this range, six phantoms with $T_2$ values spanning 30–100 ms were prepared and imaged using different echo spacings and numbers of echoes. Due to the single-shot nature of the acquisition, echo spacing is typically longer than in multi-shot sequences. An echo spacing of 25 ms was chosen to ensure a balance between multi-echo coverage and adequate in-plane spatial resolution ($0.70 \times 0.70$ mm$^2$). Accurate $T_2$ quantification requires at least three echoes and a total echo time range that adequately covers the expected $T_2$ distribution. As shown in **Figure S7B**, signal intensity decreases exponentially with increasing $TE_{eff}$ due to $T_2$ relaxation, resulting in progressively darker images and reduced signal-to-noise ratio (**Figure S7A**). Table S4 summarizes the measured $T_2$ and PD values from phantom studies using both the MP-CEST and reference spin-echo methods under different echo configurations. Considering the trade-off between fitting accuracy, signal-to-noise ratio, and acquisition efficiency, the 5-echo acquisition was identified as the optimal configuration and was adopted in the final imaging protocol.

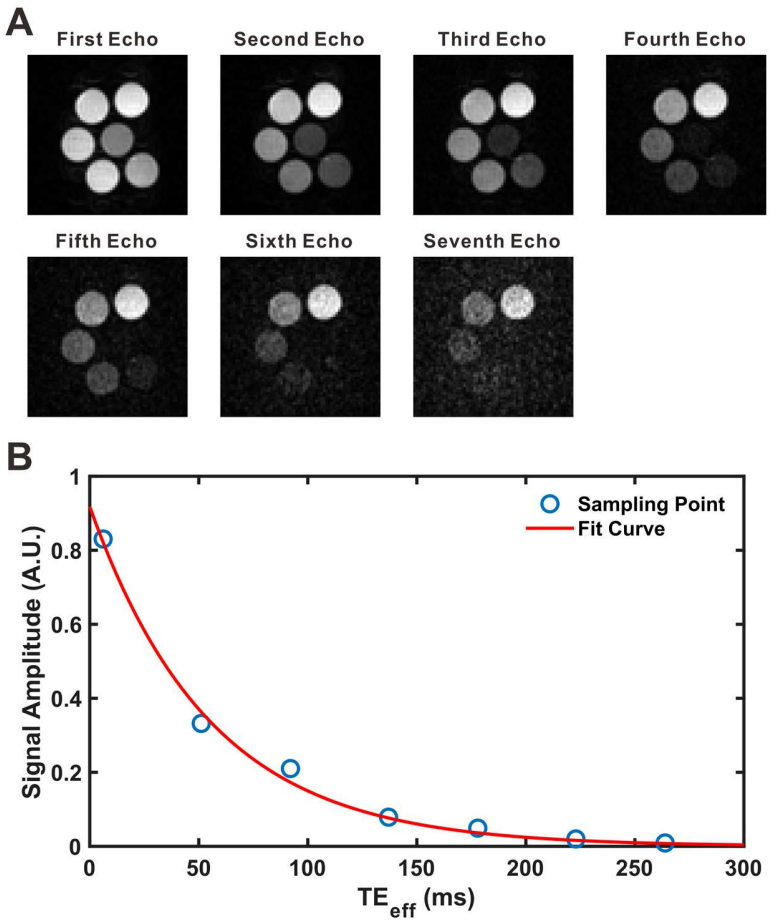


**Figure S7**. **(A)** Representative reconstructed images obtained using seven echo trains with increasing effective echo times (TEeff), illustrating progressive signal attenuation due to $T_2$ relaxation. **(B)** Acquired signal intensities (dots) across the echo train and the corresponding mono-exponential fitting curve (line).

**Table S3**. $T_2$ and PD measurements in phantoms using different numbers of echoes.

| | | MP-CEST | | | | | Reference |
|---|---|---|---|---|---|---|---|
| | | **3 shot** | **4 shot** | **5 shot** | **6 shot** | **7 shot** | |
| **Phantom 1** | **$T_2$ (ms)** | **33.21 ± 1.33** | 33.30 ± 1.35 | 33.49 ± 1.36 | 33.48 ± 1.37 | 33.51 ± 1.38 | 32.88 |
| | **PD (A.U.)** | **0.900 ± 0.043** | 0.894 ± 0.045 | 0.896 ± 0.046 | 0.895 ± 0.045 | 0.896 ± 0.045 | 0.909 |
| **Phantom 2** | **$T_2$ (ms)** | 39.04 ± 1.26 | **39.72 ± 1.26** | 40.05 ± 1.30 | 40.16 ± 1.30 | 40.22 ± 1.30 | 39.6 |
| | **PD (A.U.)** | 0.883 ± 0.045 | 0.892 ± 0.032 | **0.902 ± 0.042** | 0..900 ± 0.041 | 0.900 ± 0.041 | 0.910 |
| **Phantom 3** | **$T_2$ (ms)** | 50.09 ± 1.69 | 50.39 ± 1.56 | **50.89 ± 1.55** | 51.01 ± 1.53 | 51.11 ± 1.54 | 51.00 |
| | **PD (A.U.)** | 0.937 ± 0.043 | 0.932 ± 0.041 | **0.927 ± 0.041** | 0.927 ± 0.041 | 0.927 ± 0.041 | 0.930 |
| **Phantom 4** | **$T_2$ (ms)** | 59.5 ± 3.05 | 58.86 ± 3.15 | **60.10 ± 2.27** | 60.35 ± 2.40 | 60.51 ± 2.25 | 60.23 |
| | **PD (A.U.)** | 0.883 ± 0.071 | 0.892 ± 0.074 | **0.902 ± 0.061** | 0..909 ± 0.065 | 0.901 ± 0.071 | 0.905 |
| **Phantom 5** | **$T_2$ (ms)** | 74.42 ± 1.76 | 74.21 ± 1.40 | 75.11 ± 1.83 | **75.72 ± 1.73** | 76.45 ± 1.91 | 75.48 |
| | **PD (A.U.)** | 0.938 ± 0.034 | 0.938 ± 0.037 | **0.931 ± 0.038** | 0..942 ± 0.042 | 0.941 ± 0.038 | 0.931 |
| **Phantom 6** | **$T_2$ (ms)** | 94.74 ± 2.07 | 92.97 ± 1.45 | **94.47 ± 1.29** | 94.44 ± 1.47 | 94.75 ± 1.56 | 94.61 |
| | **PD (A.U.)** | 0.915 ± 0.018 | 0.918 ± 0.017 | **0.919 ± 0.019** | 0..917 ± 0.018 | 0.915 ± 0.021 | 0.921 |

**Supplementary Section 5. Additional saturation-weighted PD and $T_2$ mapping results**

This section presents additional saturation-weighted PD and $T_2$ maps acquired using the MP-CEST sequence, which were not included in the main text. The data include both saturated and unsaturated conditions, along with corresponding reference maps for validation. These results are shown in Supplementary **Figure S8**.

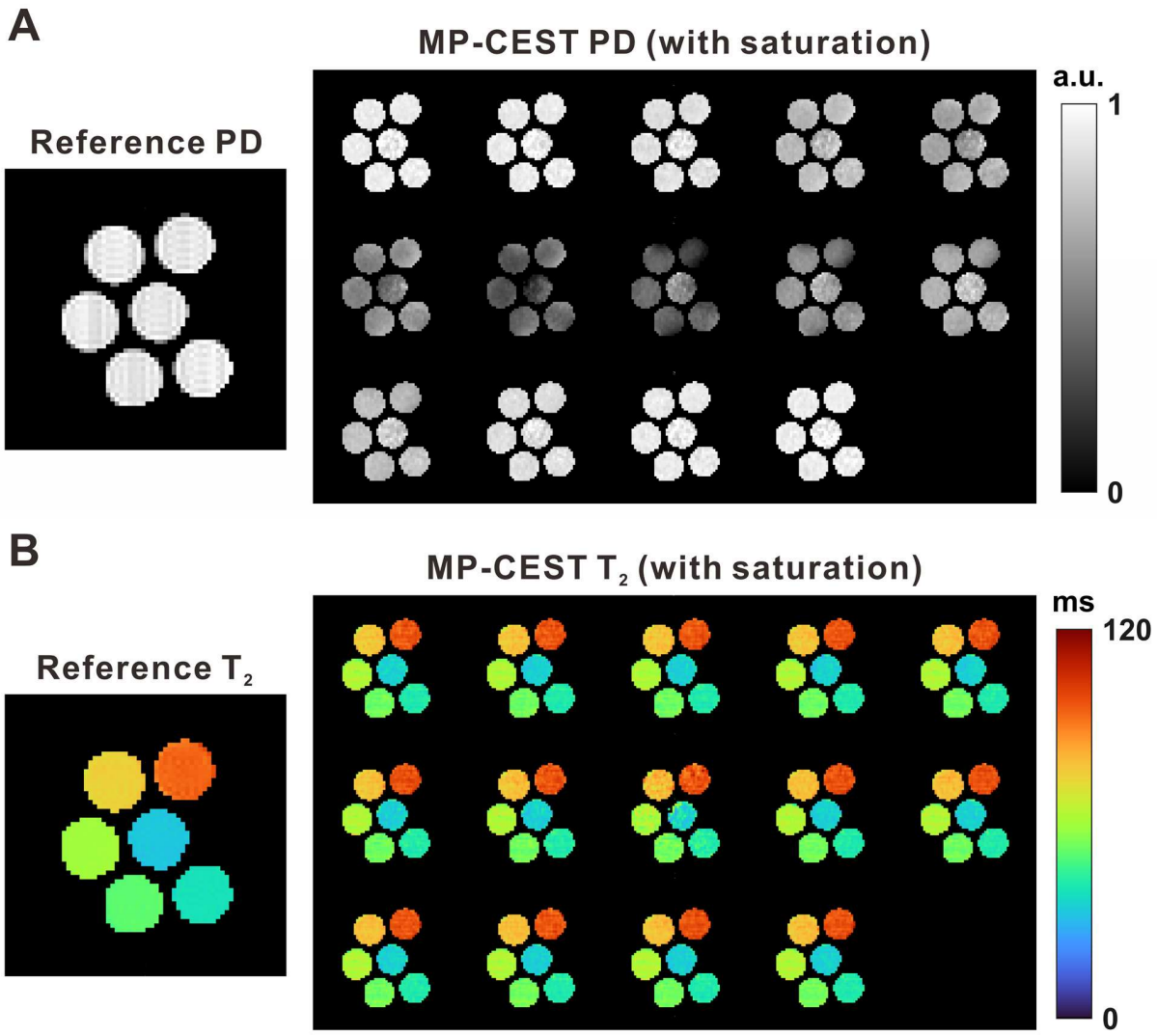


**Figure S8**. Comparison of quantitative PD and $T_2$ maps between MP-CEST MRI and reference in vitro measurements. **(A)** PD maps obtained using the MP-CEST method and the reference. **(B)** $T_2$ maps obtained using the MP-CEST method and the reference.

**Supplementary Section 6. Additional Z-spectrum and $MTR_{asym}$ results from phantom experiments**

The Z-spectrum and $MTR_{asym}$ plot for the tube containing 10 mM glucose are shown in **Figure S9**.

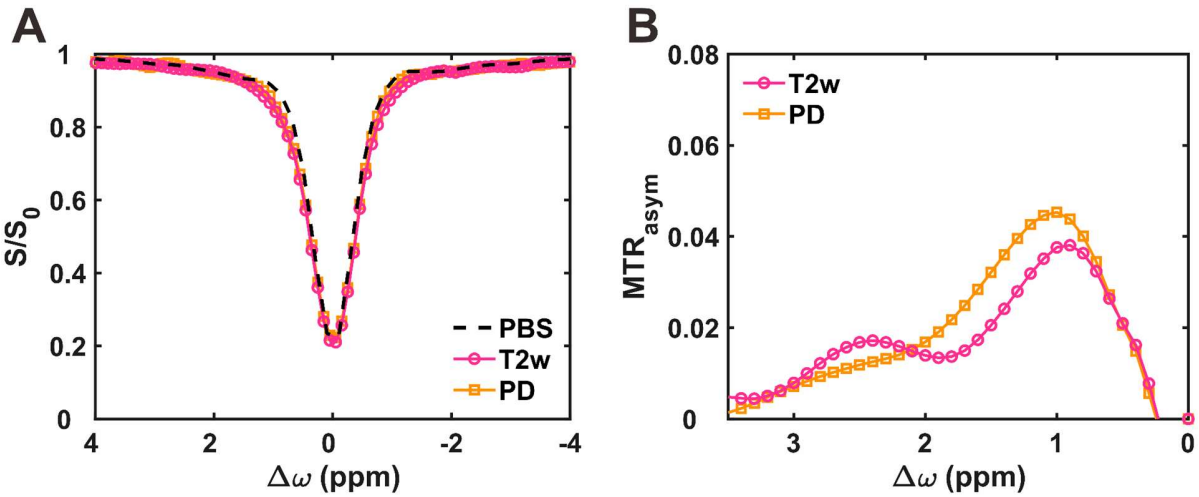


**Figure S9**. **(A)** Z-spectra derived from $T_2$-weighted images and saturation-weighted PD images at a glucose concentration of 10 mM. **(B)** Corresponding $MTR_{asym}$ plots calculated from the respective Z-spectra.

**Supplementary Section 7. Numerical Validation**

Here, a numerical simulation was performed using the parameters in **Table S2** to assess which form of transverse relaxation is more suitable for correction [3]. As shown in **Figure S10**, $T_2$ demonstrates superior linearity compared with $R_2$ under the evaluated conditions, with coefficients of determination ($R^2$) of 0.996 vs. 0.967, 0.999 vs. 0.954, 0.999 vs. 0.944, and 0.991 vs. 0.865 for $T_2$ and $R_2$, respectively.

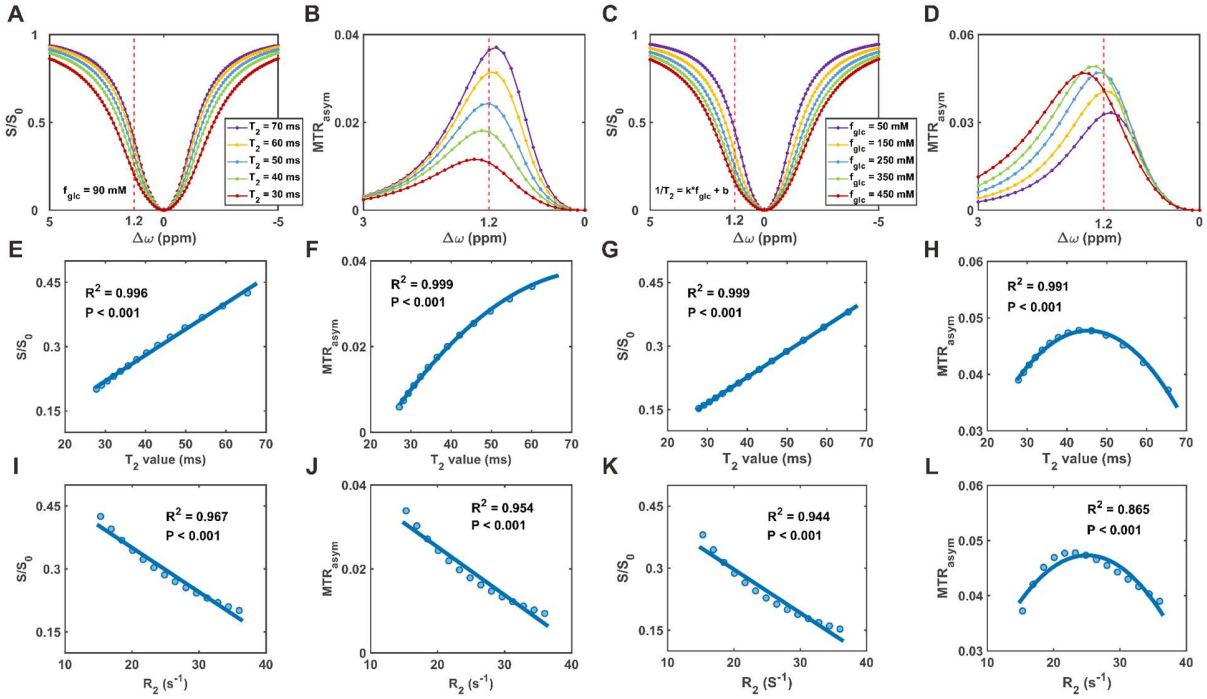


**Figure S10. Simulation of glucoCEST signal under varying glucose concentrations and transverse relaxation. (A)** Simulated Z-spectra at varying $T_2$ relaxation times. **(B)** $MTR_{asym}$ curves corresponding to (A). **(C)** Z-spectra under combined variations of $T_2$ and glucose concentration. **(B)** $MTR_{asym}$ under the same combined conditions. **(E)** Correlation between $T_2$ and $S/S_0$. **(F)** Correlation between $T_2$ and $MTR_{asym}$. **(G)** Correlation between combined $T_2$–glucose variations and $S/S_0$. **(H)** Correlation between combined $T_2$–glucose variations and $MTR_{asym}$. **(I)** Correlation between $R_2$ and $S/S_0$. **(J)** Correlation between $R_2$ and $MTR_{asym}$. **(K)** Correlation between combined $R_2$–glucose variations and $S/S_0$. **(L)** Correlation between combined $R_2$–glucose variations and $MTR_{asym}$.

**Supplementary Section 8. LCModel analysis**

As shown in **Figure 5C**, MRS spectra acquired before (blue) and after (red) D-glucose injection revealed clear spectral differences (green) within the resonance range corresponding to glucose H2–H6 protons (3.0–4.0 ppm). Based on LCModel analysis, the glucose concentration within the selected ROI increased from $1.16 \pm 0.29$ mM at baseline to $2.33 \pm 0.64$ mM after injection, yielding a mean enhancement of $1.17 \pm 0.52$ mM ($P = 0.005$, effect size = 2.357), as summarized in **Figure S11**.

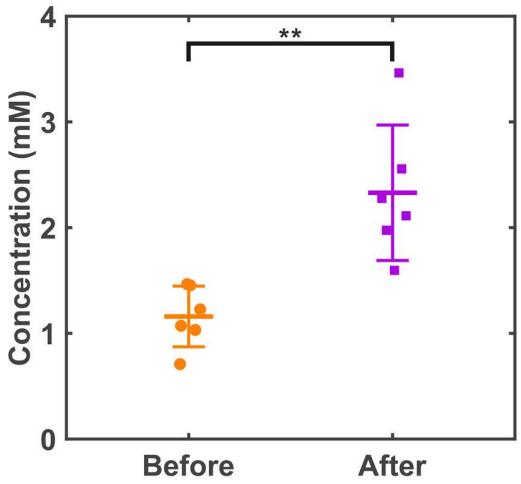


**Figure S11**. Quantification of glucose concentration before and after D-glucose injection using LCModel. Glucose levels were derived from localized MRS spectra acquired pre- and post-injection, with total creatine (tCr) serving as the internal reference. A significant increase in glucose concentration was observed following D-glucose administration ($P = 0.005$).

The MP-CEST approach was applied to correct the $T_2$-induced bias in glucose quantification. As shown in **Figure 5**, the peak single-offset DGE signal was significantly reduced from $1.62 \pm 0.19\%$ to $1.11 \pm 0.16\%$ after correction ($P = 0.009$), corresponding to an overestimation of glucose concentration by $0.54 \pm 0.34$ mM (~46%) based on LCModel analysis. Conversely, the $MTR_{asym}$ DGE signal increased from $1.29 \pm 0.20\%$ to $1.84 \pm 0.18\%$ ($P = 0.005$), indicating an initial underestimation of $0.35 \pm 0.22$ mM (~30%) prior to $T_2$ correction.

**Supplementary Section 9. Glucose uptake analysis**

To allow a quantitative comparison of dynamic glucose uptake, time-resolved signal curves in brain parenchyma were fitted using an exponential model:

$$\Delta S(t) = S_{DGE}(1 - \exp(-\mu_{in,DGE} \cdot t)) \quad \text{(S1)}$$

$$\Delta MTR_{asym}(t) = S_{MTR}(1 - \exp(-\mu_{in,MTR} \cdot t)) \quad \text{(S2)}$$

where $S_{DGE}$ and $S_{MTR}$ are the max single-offset DGE and $MTR_{asym}$ DGE signals reached, respectively. $\mu_{in,DGE}$ and $\mu_{in,MTR}$ are the glucose uptake rates by single-offset DGE and $MTR_{asym}$ DGE, respectively. Curve fitting was performed using the built-in nonlinear least-squares fitting function in MATLAB. Statistical analysis was conducted using unpaired, two-tailed Student's t-tests where appropriate. A P value < 0.05 was considered statistically significant.

As shown in **Figure S12**, the fitted $S_{DGE}$ of the original images was significantly larger than that of the corrected (1.62 ± 0.19% versus 1.11 ± 0.16%, P = 0.009), whereas the fitted $S_{MTR}$ of the original images was significantly lower than that of the corrected (1.29 ± 0.20% versus 1.84 ± 0.18%, P = 0.005). In contrast, no significant differences were observed in the uptake rates between original and corrected data: for the rate $\mu_{in,DGE}$, 0.15 ± 0.04 $min^{-1}$ versus 0.16 ± 0.05 $min^{-1}$; for the rate $\mu_{in,MTR}$, 0.16 ± 0.03 $min^{-1}$ versus 0.15 ± 0.03 $min^{-1}$.

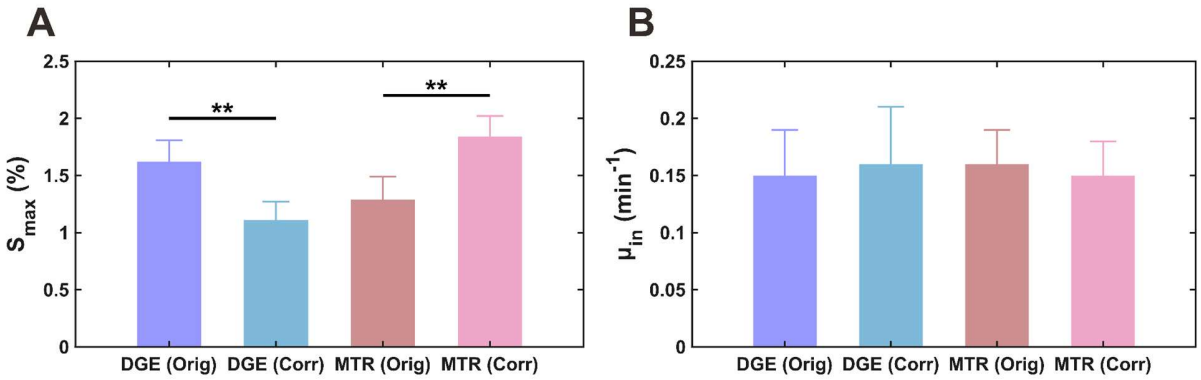


**Figure S12.** Comparison of model-fitted uptake parameters $S_{max}$ **(A)** and $\mu_{in}$ **(B)** for single-offset DGE and $MTR_{asym}$ DGE, analyzed using both the original and the $T_2$-corrected methods.

**Supplementary Section 10. Regional specificity of D-glucose uptake**

We incorporated an analysis of region-specific glucose uptake by calculating the area under the curve (AUC) for each ROI, before and after $T_2$ correction, followed by a comparative assessment across distinct brain regions. The AUC was normalized over a consistent time window to quantitatively assess the single-offset DGE signal differences:

$$AUC = \frac{\sum_{n=1}^{N} DGE_S(n)}{N} \tag{S3}$$

A regional comparison of parenchymal DGE signals is presented in **Figure S13**, where ROIs were selected from the cerebral cortex (CX, purple), hippocampus (HC, green), thalamus (TH, pink), and hypothalamus (HY, red) as shown in **Figure S13A**. To evaluate regional glucose uptake, the AUC was calculated from 2 to 35 minutes post-injection (**Figure S13B**). The results reveal a region-specific pattern of glucose uptake. Before $T_2$ correction, the hypothalamus exhibited significantly higher uptake than the thalamus (1.41 ± 0.14% vs. 1.22 ± 0.15%, $P = 0.046$), hippocampus (1.41 ± 0.14% vs. 0.96 ± 0.09%, $P < 0.001$), and cortex (1.41 ± 0.14% vs. 1.19 ± 0.11%, $P = 0.012$), consistent with its established role in metabolic regulation and glucose sensing [4, 5]. In contrast, the hippocampus demonstrated significantly lower uptake than both the thalamus ($P = 0.006$) and the cortex ($P = 0.003$). Following $T_2$ correction, although the overall AUC values were reduced, the same regional differences remained. These findings support the effectiveness of the proposed correction strategy in reducing $T_2$-related confounding and improving the regional specificity of glucose uptake assessment.

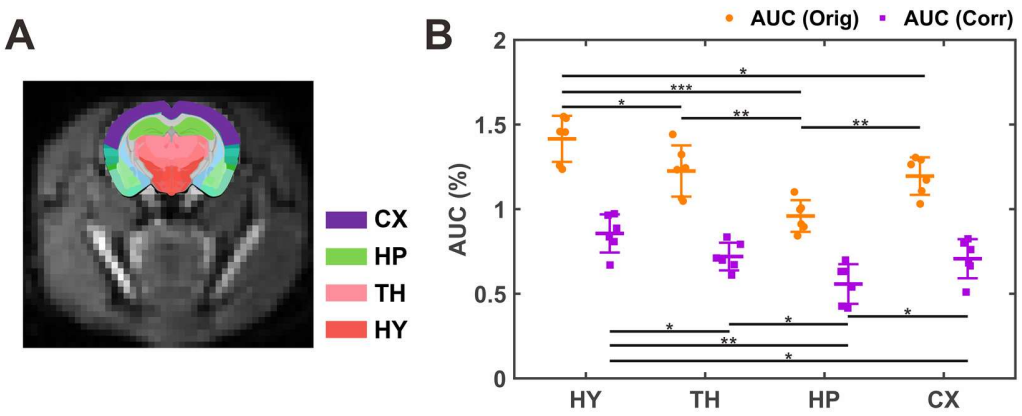


**Figure S13**. **(A)** Representative brain region segmentation for regional DGE analysis, including the cerebral cortex (CX, purple), hippocampus (HC, green), thalamus (TH, pink), and hypothalamus (HY, red). **(B)** Comparison of the area under the curve (AUC; n = 6) of the single-offset DGE signals before and after $T_2$ correction across different brain regions, calculated over the 2–35 min window following D-glucose injection.

**Supplementary Section 11. Tumor DGE and $MTR_{asym}$ signal analysis**

This section presents the dynamic single-offset DGE and $MTR_{asym}$ DGE signals observed in tumor tissue. Unlike in brain parenchyma, both signals continued to increase over time, as illustrated in Supplementary **Figure S14**.

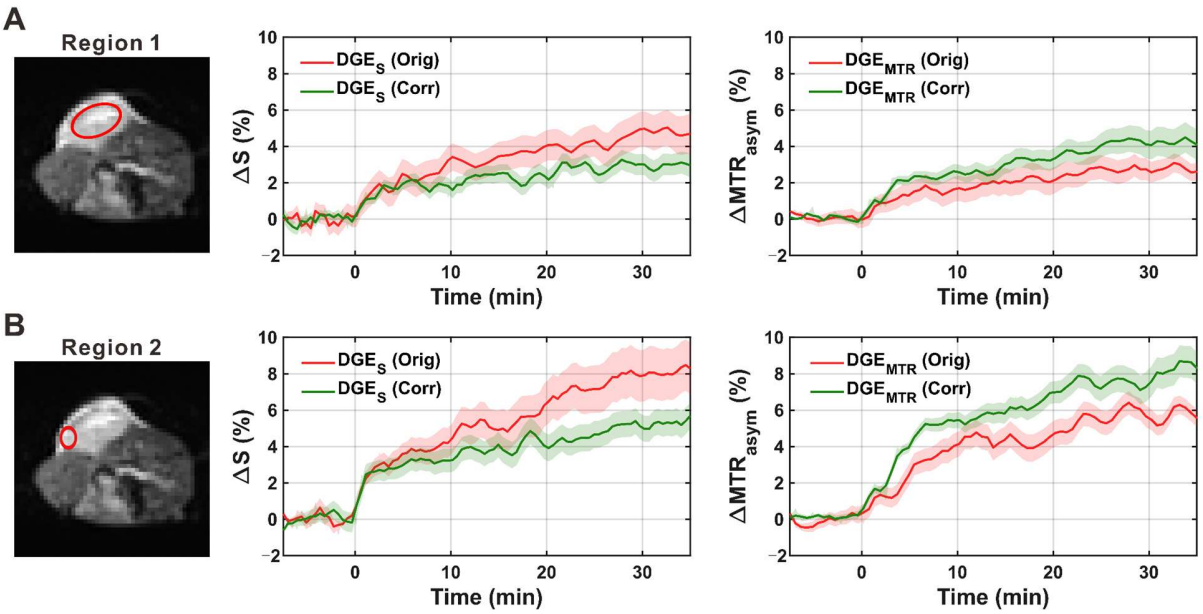


**Figure S14.** Comparisons of single-offset DGE and $MTR_{asym}$ DGE signals across different tumor regions between original and corrected datasets.

**Supplementary Section 12. $T_2$ Variations following glucose injection in tumor regions**

Following glucose infusion, a decline in $T_2$ relaxation time was observed. In the tumor, $T_2$ decreased from 47.5 ± 0.6 ms to 44.0 ± 0.8 ms in Region 1 and from 77.1 ± 3.3 ms to 62.3 ± 2.6 ms in Region 2, as shown in Supplementary **Figure S15**. These reductions reflect glucose-induced microenvironmental changes, such as enhanced chemical exchange or restricted water mobility.

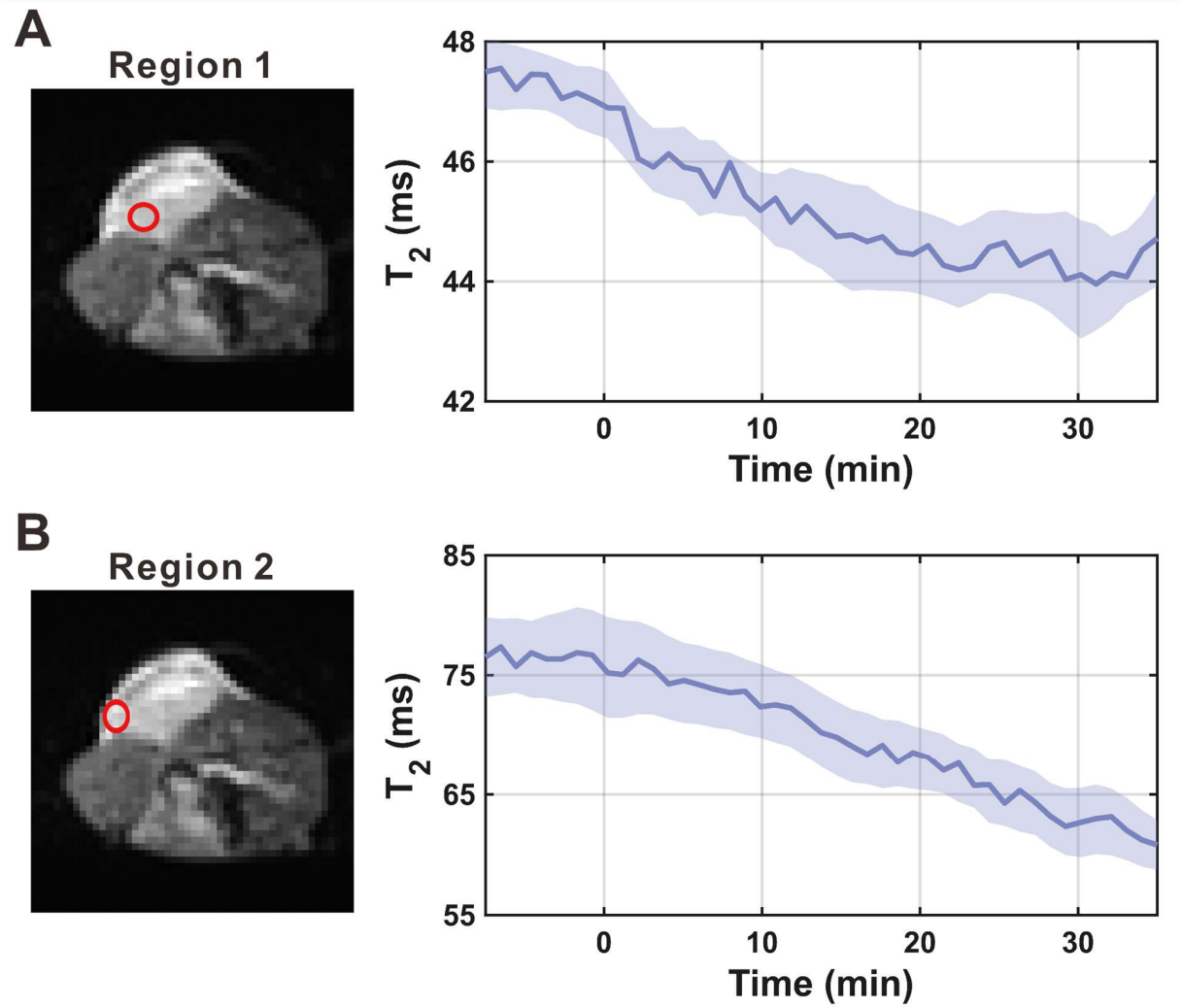


**Figure S15.** Dynamic $T_2$ curves in tumor regions following glucose injection. $T_2$ values decreased over time in both **(A)** Region 1 and **(B)** Region 2, reflecting glucose-induced relaxation changes.

**Supplementary Section 13. Influence of $T_2$ relaxation on Z-magnetization evolution**

This section illustrates the effect of $T_2$ relaxation on the temporal evolution of Z-magnetization during the CEST experiment, as shown in Supplementary **Figure S16**. The figure conceptually demonstrates how changes in $T_2$ modulate both the saturation transfer process and signal decay during acquisition, thereby introducing confounding factors into glucoCEST quantification.

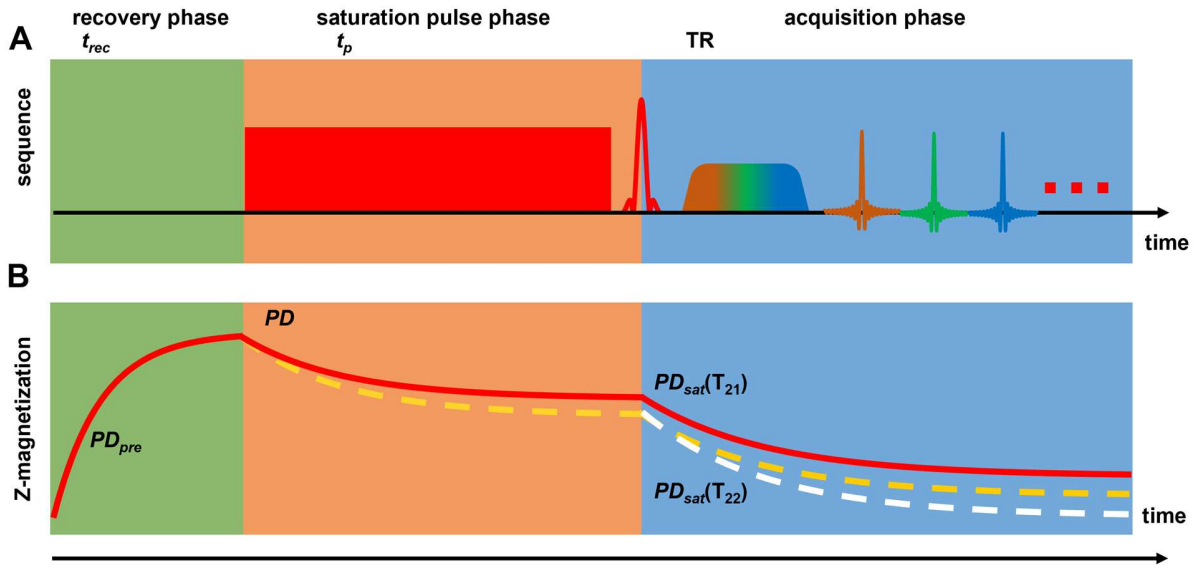


**Figure S16**. RF pulse sequence diagram **(A)** and corresponding Z-magnetization evolution **(B)** in the single-shot multiparametric CEST MRI experiment. Following the recovery interval, the Z-magnetization of the CEST-labeled acquisition ($PD_{sat}(T_{21})$, dashed yellow line) is lower than that of the reference scan without saturation (noCEST, solid red line). After glucose injection, the tissue $T_2$ decreases, leading to further attenuation of the saturated signal ($PD_{sat}$ ($T_{22}$), dashed white line), which falls below $PD_{sat}$ ($T_{21}$) at the same TE.

## References

1. Ben-Eliezer N, Irani M, Frydman L. Super-resolved spatially encoded single-scan 2D MRI. Magn Reson Med. 2010; 63: 1594-600.
2. Li J, Chen L, Cai SH, Cai CB, Zhong JH, Chen Z. Imaging with referenceless distortion correction and flexible regions of interest using single-shot biaxial spatiotemporally encoded MRI. Neuroimage. 2015; 105: 93-111.
3. Yadav NN, Xu JD, Bar-Shir A, Qin Q, Chan KWY, Grgac K, et al. Natural D-glucose as a biodegradable MRI relaxation agent. Magn Reson Med. 2014; 72: 823-8.
4. García-Cáceres C, Quarta C, Varela L, Gao YQ, Gruber T, Legutko B, et al. Astrocytic insulin signaling couples brain glucose uptake with nutrient availability. Cell. 2016; 166: 867-80.
5. Goutal S, Lancien M, Rivier F, Tournier N, Vaillend C. Brain glucose metabolism as a neuronal substrate of the abnormal behavioral response to stress in the mdx mouse, a model of Duchenne muscular dystrophy. Neurobiol Dis. 2025; 204: 106771.